Enhanced heterogeneous uptake of sulfur dioxide on mineral particles through modification of iron speciation during simulated cloud processing

Zhenzhen Wang[1], Tao Wang[1], Hongbo Fu[1, 2, 3], Liwu Zhang[1], Mingjin Tang[4], Christian George[5], Vicki H. Grassian[6], and Jianmin Chen[1]

[1]Shanghai Key Laboratory of Atmospheric Particle Pollution and Prevention, Department of Environmental Science & Engineering. Institute of Atmospheric Sciences, Fudan University, Shanghai, 200433, China

[2]Shanghai Institute of Pollution Control and Ecological Security, Shanghai 200092, China

[3]Collaborative Innovation Center of Atmospheric Environment and Equipment Technology (CICAEET), Nanjing University of Information Science and Technology, Nanjing 210044, China

[4]State Key Laboratory of Organic Geochemistry and Guangdong Key Laboratory of Environmental Protection and Resources Utilization, Guangzhou Institute of Geochemistry, Chinese Academy of Sciences, Guangzhou 510640, China

[5]University of Lyon, Université Claude Bernard Lyon 1, CNRS, IRCELYON, F-69626, Villeurbanne, France

[6]Departments of Chemistry and Biochemistry, University of California, San Diego, La Jolla, California 92093, United States

Correspondence to: Hongbo Fu (fuhb@fudan.edu.cn); Jianmin Chen (jmchen@fudan.edu.cn)

Abstract. Iron-containing mineral aerosols play a key role in the oxidation of sulfur species in the atmosphere. Simulated cloud processing (CP) of typical mineral particles, such as illite (IMt-2), nontronite (NAu-2), smectite (SWy-2) and Arizona test dust (ATD) is shown here to modify sulfur dioxide (SO_2) uptake onto mineral surfaces. Heterogeneous oxidation of SO_2 on particle surfaces was firstly investigated using an *in situ* DRIFTS apparatus. Our results showed that the BET surface area normalized uptake coefficients (γ_{BET}) of SO_2 on the IMt-2, NAu-2, SWy-2 and ATD samples after CP were 2.2, 4.1, 1.5 and 1.4 times higher than the corresponding ones before CP, respectively. The DRIFTS results suggested that CP increased the amounts of reactive sites (e.g., surface OH groups) on the particle surfaces and thus enhanced the uptake of SO_2. TEM showed that the particles broke up into smaller pieces after CP, and thus produced more active sites. The "free-Fe" measurements confirmed that more reactive Fe species were present after CP, which could enhance the SO_2 uptake more effectively. Mössbauer spectroscopy further revealed that the formed Fe phase were amorphous Fe(III) and nanosized ferrihydrite hybridized with Al/Si, which were possibly transformed from the Fe in the aluminosilicate lattice. The modification of Fe speciation was driven by the pH-dependent fluctuation coupling with Fe dissolution-precipitation repeatedly during the experiment. Considering both the enhanced SO_2 uptake and subsequent promotion of iron dissolution along with more active Fe formation, which in turn lead to more SO_2 uptake, it was proposed that there may be a positive feedback between SO_2 uptake and iron mobilized on particle surfaces during CP, thereby affecting climate and biogeochemical cycles. This self-amplifying mechanism generated on the particle surfaces may also serve as the basis of high sulfate loading in severe fog-haze events observed recently in China.

1 Introduction

Mineral dust is a major fraction of global atmospheric aerosol budget, with an estimated annual emission flux of 1000 to 3000 Tg into the atmosphere (Jickells et al., 2005; Andreae and Rosenfeld, 2008). Mineral dust aerosol mainly consists of quartz, feldspars, carbonates (calcite, dolomite), and clay minerals (illite, kaolinite, chlorite, montmorillonite), the exact composition varies with source (Claquin et al., 1999; Formenti et al., 2008; Journet et al., 2008). A long range transport would result in a decrease of quartz relative to the clay fraction because of the more rapid removal of quartz, hence clay is an important component of mineral dusts (Mahowald et al., 2005; Journet et al., 2008). During the long-range transport, mineral dust provides a reactive surface for heterogeneous chemistry (Zhang et al., 2006; George et al., 2015; Huang et al., 2015). Heterogeneous reactions of atmospheric trace gases on mineral dust particles are of great significance as these reactions alter the chemical balance of the atmosphere and modify the properties of individual particles (Usher et al., 2003; Wu et al., 2011; Huang et al., 2015).

SO_2 is an important trace gas, which is released mainly by fossil fuel combustion and volcanic emission. The heterogeneous conversion of SO_2 on mineral dust surfaces leads to the formation of sulfuric acid and sulfate aerosols, resulting in a significant cooling effect on the global climate by scattering solar radiation and acting as cloud condensation nuclei (CCN) to affect climate indirectly (Lelieveld and Heintzenberg, 1992; Usher et al., 2003; Kolb et al., 2010). In addition, sulfate containing particles play a significant role in the haze formation in China in recent years (Sun et al., 2014; Wang et al., 2014; Yang et al., 2017). SO_2 can be gaseous oxidized to sulfate by OH radical, and be aqueous oxidation in cloud and fog droplets by ozone and hydrogen peroxide (Luria and Sievering, 1991), or through heterogeneous processes that occur

74 on aerosol particle surfaces (Usher et al., 2003; Ullerstam et al., 2003). However, the

75 high sulfate levels measured in recent field observations cannot be explained by

76 current atmospheric models (Kerminen et al., 2000; Wang et al., 2003; Cheng et al.,

77 2016), leading to a large gap between the modeled and field-observed sulfate

78 concentrations using known oxidation pathways (Herman, 1991; Kasibhatla et al.,

79 1997; Barrie et al., 2016). Overall, on a global scale, atmospheric SO_2 concentration

80 were typically overestimated, while sulfate tended to be underestimated, suggesting

81 missing sulfate production pathways (Harris et al., 2013; Kong et al., 2014).

82 It has been suggested that the heterogeneous conversion of SO_2 could make an

83 important contribution to the atmospheric sulfate loading. Laboratory studies typically

84 focus on SO_2 uptake onto a variety of metal oxides and mineral particles (Goodman et

85 al., 2001; Usher et al., 2002; Zhao et al., 2015; Yang et al., 2016), and have confirmed

86 that its conversion rate on the surface of Fe (hydr)oxides was faster compared to other

87 metal oxides investigated, in good agreement with the field-measurement (Usher et al.,

88 2002; Zhang et al., 2006). Atmospheric Fe is emitted from both anthropogenic

89 (primarily biomass burning, coal and oil combustion) and natural (mineral dust and

90 volcanic ash) sources, with the mineral dust source dominant globally (Siefert et al.,

91 1998; Luo et al., 2008; Ito et al., 2019). It has been established that an important in

92 cloud S (IV) oxidation pathway is catalyzed by natural transition metal ions,

93 especially Fe hosted within mineral particles (Alexander et al, 2009; Harris et al.,

94 2013).

95 Another important consideration for heterogeneous chemistry of mineral dust

96 aerosol, is how mineral dust particles change in the atmosphere. During long-range

97 transport, mineral particles often undergo chemical ageing by atmospheric processes

98 (Mahowald et al., 2005; Baker and Croot, 2010; Shi et al., 2011). Cloud processing

99   involves cloud water condensation and evaporation on the particle surfaces, along

100 with drastic liquid water content and pH fluctuations (Mackie, 2005; Shi et al., 2011;

101 Rubasinghege et al., 2016). During CP, the high relative humidity (RH) results in high

102 aerosol water content and relatively high pH (Behra et al., 1989; Baker and Croot,

103 2010; Shi et al., 2011). While water evaporation from cloud droplets to wet aerosol at

104 higher temperature, the particles only contain a concentrated aqueous aerosol solution,

105 in which the pH can be lower than 2 (Zhu et al., 1993; Meskhidze, 2003; Shi et al.,

106 2015). Therefore, there is a highly acidic film (e.g., pH = 2) in the "wet aerosol" phase

107 versus a less acidic droplet (near-neutral, 5-6) in the "cloud droplet" phase within

108 clouds (Shi et al., 2015). During its lifetime, a typical aerosol particle may experience

109 several cloud cycles involving large pH variations before being removed from the

110 atmosphere as rain or through dry deposition (Pruppacher and Jaenicke, 1995; Maters

111 et al., 2016). Herein, the simulated CP experiment was conducted by changing pH

112 between 2 and 5-6, in accordance with the previous studies (Spokes et al., 1994;

113 Mackie, 2005; Shi et al., 2009).

114   It was well documented that pH is especially important for Fe mobilization (Zhu et

115 al., 1993; Desboeufs et al., 2001; Deguillaume et al., 2010; Maters et al., 2016). The

116 fluctuating pH during CP will impact and change the Fe speciation and morphology in

117 dust particles (Zhuang et al., 1992; Wurzler et al., 2000; Shi et al., 2009; Kadar et al.,

118 2014). The low pH will increase Fe solubility and bioavailability of dust during

119 transport, thereby providing Fe external input to the open ocean surface to promote

120 marine prime productivity (Spokes et al., 1994; Desboeufs et al., 2001). It has been

121 found that Fe-rich nanoparticle aggregates were formed from Saharan soil and

122 goethite upon simulated CP conditions, in good agreement with their

123 field-measurements from the wet-deposited Saharan dusts collected from the western

124 Mediterranean (Shi et al., 2009). Fe nanoparticles are more chemically reactive

125 (Wurzler et al., 2000; Desboeufs et al., 2001), possibly lead to a remarkable difference

126 in heterogeneous chemistry. However, little is known about the influence of CP on

127 SO_2 uptake onto particle surfaces up to now.

128 In this study, we employed four typical Fe-containing mineral samples as

129 surrogates to perform simulated CP experiments. The SO_2 uptakes on the mineral

130 particles before and after CP were compared using *in situ* diffuse reflectance infrared

131 Fourier transform spectroscopy (DRIFTS). Transmission electron microscopy (TEM)

132 was applied to observe the morphological and mineralogical change of mineral

133 particles. The Fe speciation modification during simulated CP was further monitored

134 by the dissolved Fe measurement, the "free-Fe" analysis and Mössbauer spectroscopic

135 characterization.

136 **2   Material and methods**

137 **2.1 Mineral particles**

138 The standard mineral samples of IMt-2, NAu-2 and SWy-2 were purchased from

139 the Source Clay Minerals Repository (Purdue University, West Lafayette, IN). ATD

140 was purchased from Powder Technology Inc. (Burnsville, MN, USA). The mineral

141 samples were coarsely ground using a mortar and pestle before being more finely

142 ground using an All-dimensional Planetary Ball Mill QM-QX (Nanjing University

143 Instrument Plant) and were sieved to particle diameters (D_p) < 45 μm prior to analysis.

144 The Brunauer-Emmett-Teller specific surface areas (S_{BET}) of the samples were

145 measured with a Quantachrome Nova 1200 BET apparatus. Total iron content (Fe_T) of

146 the samples were determined using an inductively coupled plasma atomic emission

147 spectroscopy (ICP-AES, Jobin Yvon Ultima). The chemical compositions of the

148 particles were analyzed by X-ray fluorescence spectrometry (XRF, PANalytical Axios

149   Advanced).

2.2 Cloud processing simulation experiment

151   The simulated CP experiments were conducted at a constant temperature ($298 \pm 1K$)

152   using a Pyrex glass vessel with a water jacket. The suspensions contained a mineral

153   particle loading of 1 g L^{-1} were subjected to acidic (pH = 2 ± 0.1, 24 h) and

154   near-neutral pH (pH = 5-6, 24 h) cycles for 1-3 times according to the previous

155   methods (Spokes et al., 1994; Mackie, 2005; Shi et al., 2009). Suspension pH was

156   adjusted by adding dilute H_2SO_4 or NH_4OH. The $CaCO_3$ equivalent alkalinity of the

157   dust was determined in accordance with APHA method 2320B so that acid additions

158   to control pH could be adjusted accordingly (Mackie, 2005). The amount of acid or

159   alkali added to achieve these pH cycles was less than 1% of the total volume of the

160   suspensions. The experiments were performed under a constant stirring (about 50

161   rpm) in the dark for 144 h. At the end of the CP experiment, the suspensions were

162   filtered through 0.2 μm PTFE filters (Millipore). The filter residue was air-dried, and

163   was further applied to the DRIFTS experiment, as well as TEM observation, "free-Fe"

164   measurement and Mössbauer spectroscopic characterization.

2.3 SO$_2$ uptake on the mineral particles

166   The SO$_2$ uptake on the particle surfaces before and after CP was investigated by a

167   Shimadzu Tracer-100 FTIR spectrometer equipped with a high-sensitivity mercury

168   cadmium telluride (MCT) detector and a diffuse reflectance accessory. A temperature

169   controller was fitted to the DRIFTS chamber to ensure constant reaction temperature

170   (298 K). Weighted sample was placed into a ceramic crucible (0.35 mm depth, 5 mm i.

171   d.) in the chamber. Mass flow controllers (Beijing Sevenstar electronics Co., LTD)

172   were used to adjust the reactant gases to a flux with expected concentration and

173   relative humidity. The sample was firstly pretreated in a 100 mL min^{-1} flow of

synthetic air (21% O_2 and 79% N_2) for 1 h to blow off water and impurities on particle surface. When the background spectrum of the fresh sample reached steady state, the reactant gas of SO_2 (5.0 ppm) along with synthetic air was introduced into the chamber at a total flow rate of 120 mL min^{-1} for 45 min, during which the IR spectrum was recorded automatically every 5 min at a resolution of 4 cm^{-1} for 100 scans in the spectral range of 900 to 4000 cm^{-1}. Atmospheric moisture was simulated with a RH level around 40 % by guiding one high-pure air flux through water. The humidity value was monitored using a hygrometer.

The sulfate products were analyzed by ion chromatography (IC) after the DRIFTS experiments. The particles were extracted with 5 ml ultrapure water by ultrasonic extractor. After 10 min, the extracted solution was passed through a 0.22 μm PTFE membrane filter and the leaching solution was analyzed using a Metrohm 883 Basic IC equipped with an A5-250 column. A weak base eluent (3.2 mmol L^{-1} Na_2CO_3 plus 1.0 mmol L^{-1} $NaHCO_3$) was used for anion detection at a flow rate of 0.70 ml min^{-1}. To discriminate the adsorbed sulfate during simulated CP experiment and the sulfate ions generated from the heterogeneous reaction, the adsorbed sulfate on the particles during simulated CP experiment were initially measured as blank. The heterogeneous uptake of SO_2 was calculated by subtracting the blank value from the total sulfate ions.

The reactive uptake coefficient (γ) was defined as the rate of sulfate formation on the surface (d[SO_4^{2-}]/dt, ions s^{-1}) divided by collision frequency (Z, molecules s^{-1}) (Usher et al., 2003; Ullerstam et al., 2003; Kong et al., 2014; Huang et al., 2015).

$$\gamma = \frac{d[SO_4^{2-}]/dt}{Z}, \qquad (1)$$

$$Z = \frac{1}{4} \times A_s \times [SO_2] \times v, \qquad (2)$$

198
$$v = \sqrt{\frac{8RT}{\pi M_{SO_2}}}, \qquad\qquad (3)$$

199   Where, A_s is the effective sample surface of the samples, m^2; v is the mean

200 molecular velocity of SO_2, m s^{-1}; R is the gas constant, J mol K^{-1}; T is the absolute

201 temperature, K; and M_{SO_2} is the molecular weight of SO_2, kg mol^{-1}.

202   A conversion factor was obtained by a calibration plot with numbers of SO_4^{2-}

203 analyzed by ion chromatography (IC, Metrohm 883 Basic, Switzerland) versus the

204 integrated areas of sulfate products from DRIFTS spectra. The residual sulfate during

205 simulated CP experiments were deducted as background. The calculated conversion

206 factor of SO_4^{2-} is 1.170×10^{15} (ions · integrated $units^{-1}$). Integrated areas for the total

207 sulfur-containing products were calculated to show the maximal sulfate formation

208 rates. The reactive uptake coefficient for SO_2 was determined to be γ_{BET} and γ_{geo} using

209 the BET area ($A_{BET} = mass \times S_{BET}$) and geometric area ($A_{geo} = mass \times S_{geo}$) as the

210 reactive area, respectively.

211 **2.4 Morphological and mineralogical characterization of the Fe speciation**

212   A FEI TECNAI G2 S-TWIN F20 TEM equipped with an Oxford energy-dispersive

213 X-ray spectrometer (EDX) was used to analyze the morphological and chemical

214 composition of individual particles before and after CP. Suspensions (0.2 g L^{-1}) of

215 each particle were prepared in methanol and sonicated for at least 1 h. A drop of this

216 suspension was then applied to a carbon-coated Cu TEM grid (400 mesh; EMS) and

217 allowed to air-dry. The operation was conducted in bright field mode at 120 kV. The

218 Fe content of the typical individual mineral particle were calculated from the values

219 of 50 typical particles. To obviously observe the morphological changes,

220 high-resolution TEM (HRTEM) images were also collected to observe nanoscale

221 structural features, e.g., surface roughness and lattice fringes.

222   The content of "free-Fe" in the mineral particles was determined by a

223   citrate-buffered-dithionite (CBD) sequential Fe extractions method according to the

224   literature (Lafon et al., 2004; Shi et al., 2009). Simply, 30 mg of the dust samples

225   were treated for 24 h with a 10 mL ascorbate solution (pH = 7.5) to extract chemically

226   highly labile Fe phases (Fe_A), mainly composed of amorphous, nanoparticle and/or

227   poorly crystalline ferrihydrite. The solutions were filtered through 0.2 μm

228   polycarbonate filters. The dust particles collected on the filters were subsequently

229   treated for 2 h with a 10 mL sodium dithionite solution (pH = 4.8) to extract

230   crystalline Fe (oxyhydr) oxides (Fe_D), which are mainly goethite and hematite. After

231   each reaction step, the dissolved Fe concentrations (Fe_A and Fe_D) in the filtrates were

232   determined using ICP-AES. The sum of these two pools ($Fe_A + Fe_D$) was defined as

233   the "free-Fe" fraction (Shi et al., 2011). The other fraction was donated as the

234   "structural-Fe" in aluminosilicate crystals, which could be calculated from the

235   difference between the Fe_T and "free-Fe" fractions (Lafon et al., 2004).

236   The Mössbauer spectroscopic analysis performed in transmission geometry with a

237   constant acceleration was used to inspect the chemical valence and the surrounding

238   structure of Fe in the particles before and after CP. [57]Co was used as the Mössbauer

239   source, and a 1 mm thick Na(TI) scintillator coupled to a EMI9750B photoelectric

240   multiplier was used as the detector (Cwiertny et al., 2008). The measurement was

241   carried out at room temperature (RT) with a duration of 24 hours for one sample

242   (around 1.5×10^6 counts per channel). Experimental data were fitted by a least-squares

243   fitting-program. The isomer shift values were calibrated against a spectrum for α-Fe

244   metal foil.

245   During the simulated CP experiment, the total dissolved iron (Fe_s) and the dissolved

246   Fe(II) in the suspensions were measured colorimetrically by the Ferrozine method, as

247   described in previous studies (Viollier et al., 2000; Cwiertny et al., 2008). For Fe(II)

248   analysis, 200 mL of a 5 mM 1, 10-phenanthroline solution and 200 mL of an

249   ammonium acetate buffer were added into 1 mL of sample. To avoid possible

250   interference from Fe(III), which can also form a complex with 1,10-phenanthroline

251   when present at high concentrations, 50 mL of 0.43 M ammonium fluoride was added

252   to the sample prior to 1,10-phenanthroline. The mixture was allowed to sit in the dark

253   for 30 min prior to ultraviolet-visible spectroscopy (UV-Vis) analysis, during which

254   time a reddish-orange color developed if Fe(II) was present. Fe_s was determined via

255   the same protocol, except that 20 mL of 1.5 M hydroquinone, which reduces Fe(III) to

256   Fe(II), was added to the sample rather than ammonium fluoride. Absorbance

257   measured at 510 nm was converted to concentrations using aqueous standards

258   prepared from anhydrous beads of ferrous chloride. Standards were prepared in each

259   acid used in dissolution studies, and no matrix effects were observed. These

260   conditions resulted in a detection limit of 1 μM. The concentration of dissolved

261   Fe(III) was calculated from the difference in experimentally measured concentrations

262   of total dissolved iron and dissolved Fe(II).

263   Additionally, the dissolved Fe(III) could precipitate out as the pH increased, and

264   then the Fe mineraology of the deposit was also observed. NAu-2 released about

265   300 μM of dissolved Fe at pH 2. The dissolving solution (200 mL) was sampled

266   after filtration (0.2 μm polycarbonate filter). The clear solution was subjected to

267   changing acidity from pH 2 to 5 by the stepwise addition of dilute NH_4OH. The

268   precipitated particles were separated out by 0.2 μm filters and were used in TEM

269   and Mössbauer analysis. Size distributions for the Fe-bearing particles formed in

270   the suspensions were determined by a Horiba LB-500 light scattering microscopy

271   within the size range of 3-6000 nm.

3 Results and discussion

3.1 Morphological change of the mineral particles after CP.

The characteristic results are shown in Table S1 and Table S2. The samples exhibited S_{BET} in the range from 4.3 ± 0.3 to 22.6 ± 2.3 m^2/g. The Fe$_T$ content were $5.45\pm0.34\%$, $26.30\pm0.57\%$, $2.36\pm0.56\%$ and $1.48\pm0.56\%$, for IMt-2, NAu-2, SWy-2 and ATD, respectively. The proportions of Fe$_2$O$_3$ in IMt-2, NAu-2, SWy-2 and ATD were 7.95%, 39.03%, 5.55% and 2.57%, respectively.

Figure 1 shows the TEM images of the mineral particles before and after CP. As shown in Figure 1 a, c, e and g, the IMt-2, NAu-2, SWy-2 and ATD samples before CP primarily consisted of laminar aluminosilicate with irregular shape and rough morphologies mainly at the micrometer scale, all of which were characterized by various fractions of Fe (1.5%-26.2%), along with minor Mg (0.1%-16.5%), K (0.0%-7.8%) and Ca (0.0%-1.1%). The Fe within the aluminosilicates of the particles was evenly distributed. Besides, some Fe-rich crystal with several hundreds of nanometers in size were found to attach onto the ATD particles, which were identified as α-Fe$_2$O$_3$ (PDF: 33-664) from the typical d-spacing analysis of HRTEM (Janney et al., 2000).

After the simulated CP, all of the processed mineral particles showed much smaller size than the ones before CP. For example, the typical IMt-2 and NAu-2 particles after CP (Figure 1 b and d) were < 1 μm in size. Under the TEM, the average Fe content of the individual IMt-2 and SWy-2 particles (Figure 1 b and f) decreased from 5.5% ($\pm$ 1.9%; n = 50) to 4.1% ($\pm$ 1.6%; n = 50) and from 2.4% ($\pm$ 0.6%; n = 50) to 2.1% ($\pm$ 0.5%; n = 50), respectively. In addition, the IMt-2 particles after CP showed a heterogeneous distribution of the Fe on the basis of the EDX data. Most of the aluminosilicate in IMt-2 after CP hosted lower Fe content (4.1%), whereas a few of

297   the Fe-rich particles with less Si/Al were observed with irregular shapes at the

298   nanoscale. The TEM images of the NAu-2 and ATD particles after CP (Figure 1 h)

299   showed some pseudohexagonal nanoparticles with around 5 nm in diameter. Based on

300   the EDX and SAED analysis, these nanoparticles were Fe-rich and the *d*-spacings was

301   at about 1.5-2.5 Å, all of which were identified to be 2-line ferrihydrite (Janney et al.,

302   2000; Shi et al., 2009).

303   The TEM observation suggested that CP induced the disintegration of mineral

304   particles and thus produced enhanced surface area, resulting in more active sites

305   available on the particle surfaces for SO_2 uptake. Results of TEM also showed that CP

306   influenced the Fe mineralogy, and lead to the Fe-rich nanoparticle formation, which

307   could partly explain the higher SO_2 uptake on the mineral particles after CP.

308   **Figure 1**

309   **3.2 Effect of simulated CP on heterogeneous transformation of SO_2**

310   The *in situ* DRIFTS spectra on the IMt-2, NAu-2, SWy-2 and ATD samples before

311   and after CP exposed to SO_2 as a function of time are shown in Figure 2. For the

312   IMt-2 sample before CP (Figure 2a and b), the intensities of the broad peaks from

313   3600 to 3000 cm^{-1} and a weak peak at 1650 cm^{-1} increased with time. The band

314   between 3600 and 3000 cm^{-1} was attributed to the vibrations of hydrogen-bonded

315   hydroxyl species (Zhao et al., 2015), while the absorption peak at 1650 cm^{-1} was

316   mainly associated to H_2O produced from the reaction between SO_2 and surface

317   hydroxyls (Nanayakkara et al., 2012; Cheng et al., 2016). A weak vibration was

318   observed at around 1100 cm^{-1}, which might be attributed to free sulfate anions on the

319   particle surface (Ullerstam et al., 2003; Nanayakkara et al., 2012; Yang et al., 2016).

320   Previous studies established that various types of surface OH groups are the key

321   reactive sites for sulfite/sulfate and bisulfite/bisulfate formation on mineral oxides

322   (Faust et al., 1989; Usher et al., 2003; Ullerstam et al., 2003), because of the

323   complexes formed between sulfite/sulfate species and the surface OH. Generally, the

324   SO_2 adsorption grow in intensity with decreasing OH stretching and H_2O banding

325   (Zhang et al., 2006). However, the OH peaks herein were not observed to decrease

326   with prolonged time, because the losses of H_2O and OH groups on the particle

327   surfaces were replenished by maintaining the constant RH in this study.

328   When the same set of experiments were carried out using the IMt-2 sample after CP

329   (Figure 2b), the intensities of the prominent peaks were significantly higher than those

330   on the IMt-2 sample before CP. Four new bands were readily observed at 1167, 1100,

331   1088 and 1077 cm^{-1}. The new bands were easily assigned to the stretching motion of

332   surface-coordinated sulfate species (1167 cm^{-1}), i.e., bidentate surface sulfate

333   complexes, free sulfate ion (1100 cm^{-1}), and sulfite/bisulfite species (1088 and 1077

334   cm^{-1}) (Peak et al., 1999; Ullerstam et al., 2003; Yang et al., 2016). These new bands

335   remained when an argon blow-off process was carried out, suggesting that the

336   surface-adsorbed sulfite/sulfate species between 1250 and 1000 cm^{-1} was

337   chemisorbed (Zhang et al., 2006).

338   Upon adsorption of SO_2 on the surface of the NAu-2 sample before CP (Figure 2c

339   and d), the broad band from 3600 to 2800 cm^{-1} and the peaks at 1580 and 1675 cm^{-1}

340   increased drastically with time. These absorbance bands were all attributed to the

341   surface hydroxyl species (OH) and H_2O. No peaks were observed over the range of

342   1000 to 1250 cm^{-1}, suggesting that the sulfite/sulfate products were not formed newly

343   on the surface of the NAu-2 sample before CP. Upon adsorption of SO_2 on the surface

344   of the NAu-2 sample after CP (Figure 2d), the new bands at 3661 and 3450 cm^{-1}, the

345   broad band between 3400 and 2700 cm^{-1}, and the broad band centered at 2131 cm^{-1},

346   were observed as the exposure time increased. In detail, the band at 3661 cm^{-1} could

347   be assigned to stretching vibration modes of isolated or bridged surface hydroxyl

348   groups bonded to the surface iron ions embedded in the octahedral and tetrahedral

349   sites (Faust et al., 1989; Nanayakkara et al., 2012; Zhao et al., 2015). The peaks at

350   around 3450 cm^{-1}, 2131 cm^{-1} and the band between 3400 and 2700 cm^{-1} were all

351   attributed to surface OH groups (Ma et al., 2010; Zhao et al., 2017). These new bands

352   generated on the processed NAu-2 particles suggested that CP changed the location of

353   diverse OH groups on the particle surfaces. Over the range of 1250-1000 cm^{-1}, the

354   new bands centered at 1170 cm^{-1} was assigned to the asymmetric stretching of sulfate

355   (Kong et al., 2014; Yang et al., 2015).

356   The spectra of the SWy-2 samples before and after CP (Figure 2e and f) showed a

357   similar spectral character with those of the NAu-2 samples. The spectra for the ATD

358   samples before and after CP (Figure 2g and h) were roughly the same as the ones for

359   IMt-2. All of the results demonstrated that the characteristic peaks for the active OH

360   sites and the sulfite/sulfate products on the mineral particles after CP were

361   significantly higher than those on the ones before CP, indicating the higher

362   hygroscopicity and more SO_2 uptake on the particles after CP. The data shown herein

363   confirmed that CP could potentially promote the transformation of SO_2 on the particle

364   surfaces.

365   **Figure 2**

366   **3.3 Uptake coefficient of SO$_2$ on the mineral particles before and after CP**

367   The areas of the bands (from 1250 to 1000 cm^{-1}) attributed to the sulfite/sulfate

368   products as a function of time are shown in Figure 3. It was evident that the peak

369   areas of the products on the mineral particles after CP were generally greater than the

370   ones before CP. The reaction on the sample surfaces was practically saturated to SO_2

371   uptake within 15 min, except for the NAu-2 and IMt-2 samples after CP. As for all of

372 the sample, the saturation coverages of the sulfite/sulfate products after CP were

373 obviously greater than the corresponding values before CP, suggesting that CP

374 favored the sulfate formation on the mineral surfaces due to improving active site

375 number, as expected previously.

376 **Figure 3**

377 The maximum uptake coefficients (γ_{geo} and γ_{BET}) for SO_2 uptake on the samples

378 were estimated on the basis of the sulfate formation rates in the initial 15 min. The

379 values on the mineral samples before and after CP are shown in Table 1. The γ_{geo}

380 values of SO_2 on the IMt-2, NAu-2, SWy-2 and ATD samples before CP were

381 1.03×10^{-7}, 0.30×10^{-7}, 1.72×10^{-7} and 1.37×10^{-7}, respectively, which were in the order

382 of SWy-2, ATD, IMt-2 and NAu-2. The γ_{geo} values of SO_2 on the IMt-2, NAu-2,

383 SWy-2 and ATD samples after CP were 4.7, 19.4, 2.7 and 2.0 times higher than the

384 values before CP, respectively, suggesting that the SO_2 uptake on the mineral particles

385 significantly increased after CP.

386 **Table 1**

387 A_{BET} was more appropriate to represent the effective area, because the reactant may

388 diffuse into tiny holes of the entire sample. The γ_{BET} values of SO_2 on the IMt-2,

389 NAu-2, SWy-2 and ATD samples before CP were 2.62×10^{-12}, 0.75×10^{-12}, 3.70×10^{-12}

390 and 1.61×10^{-11}, respectively, which were in the order of ATD, SWy-2, IMt-2 and

391 NAu-2. It was noteworthy that the S_{BET} of samples increased after CP, as shown in

392 Table 1. The γ_{BET} values of SO_2 on the IMt-2, NAu-2, SWy-2 and ATD after CP were

393 2.2, 4.1, 1.5 and 1.4 times higher than the values before CP, respectively. The

394 discrepancies in the γ_{BET} value confirmed that the higher sulfate formation rates of the

395 particles after CP was not only due to the increased surface area of the particles, but

396 also resulting from the chemical modification on the particle surfaces.

397   The estimated uptake coefficients were several orders of magnitude lower than the

398   results from Ullerstam et al. (2003) and Usher et al. (2003), which could be partly

399   explained by the difference in the preparation of mineral dust samples, or the

400   difference between diverse experimental structures such as the DRIFTS and Knudsen

401   cell in kinetics discussion. In this study, mineral dust particles were in a highly

402   accumulative state in the sample support of Knudsen cell. The many layers of

403   particles in the latter study will hinder the diffusion of gas into the underlayer

404   particles, resulting in the underestimate of γ_{BET}. However, the values herein were

405   comparable to those obtained by the similar DRIFTS setup (Fu et al., 2007),

406   indicating the reliability of our measurements.

407   In addition, the formation rate of sulfate appeared a linear increasing trend as a

408   function of pH cycles. Specifically, the increasing amount of sulfate ions for the

409   IMt-2, NAu-2, SWy-2 and ATD samples after each pH cycle during CP were 7.0×10^{10},

410   1.0×10^{11}, 5.0×10^{10}, 3.0×10^{10}, in the order of NAu-2 > IMt-2 > SWy-2 > ATD (Figure

411   4). The multiples factors for γ_{BET} (γ_{geo}) were coincided with the total Fe content of

412   these samples: NAu-2 (26.30%) > IMt-2 (5.45%) > SWy-2 (2.36%) > ATD (1.48%).

413   We thus supposed that the SO_2 uptake on these dust samples was closely related to the

414   Fe hosted in the particles.

415   **Figure 4**

416   **3.4 Fe speciation analysis before and after CP.**

417   The fractions of "free-Fe" (including Fe_A and Fe_D) and "structural-Fe" in the

418   mineral particles before and after CP were determined by the CBD extraction (Figure

419   5). In terms of total Fe, the amorphous Fe (Fe_A) (e.g., nanoparticulate and poorly

420   crystalline ferrihydrite) contents of the IMt-2, NAu-2, SWy-2 and ATD samples

421   before CP were 0.7%, 0.5%, 0.7% and 3.8%, respectively. The crystalline Fe

422   (oxyhydr)oxides (Fe_D) (e.g., α-FeOOH and α-Fe_2O_3) contents of the IMt-2, NAu-2,

423   SWy-2 and ATD samples before CP were 7.2%, 2.3%, 4.5% and 35.5%, respectively.

424   As a result, the fractions of "structural-Fe" before CP were 92.1%, 97.2%, 94.8% and

425   60.7%, respectively, for IMt-2, NAu-2, SWy-2 and ATD.

426   After CP, the Fe_A contents of the IMt-2, NAu-2, SWy-2 and ATD samples reached

427   1.8%, 1.2%, 1.7% and 24.2%, respectively, which increased by 2.6, 2.4, 2.4 and 6.4

428   times as compared to the ones before CP. The crystalline Fe (oxyhydr)oxides (Fe_D)

429   contents of the samples after CP were not significantly changed as compared to the

430   ones before CP; whereas the content of "structural-Fe" in the Al-Si crystals of the

431   IMt-2, NAu-2, SWy-2 and ATD samples after CP decreased by various degrees, to

432   91.1%, 96.1%, 93.2% and 42.5%, respectively. Previous research had indicated that

433   Fe_A increased as a result of the simulated CP (Shi et al., 2009). Herein, we further

434   proposed that the increased fractions of Fe_A could be mostly transformed from the

435   "structural-Fe" in the aluminosilicate phase of the particles during CP, which is in

436   good agreement with the TEM observation. For example, the Fe_A in the ATD samples

437   increased from 3.8% to 24.2% after CP, accompanied by a sharp decrease of the

438   structural-Fe content from 60.7% to 42.5%.

439   **Figure 5**

440   The Mössbauer spectra and their fitted results are shown in Figure 6. The

441   corresponding hyperfine parameters estimated from the best fitted spectra are

442   presented in Table S3. The central doublet with isomer shift (IS) of 0.37 mm s^{-1} and

443   quadrupole shift (QS) of 0.72 mm s^{-1} were typical for high-spin Fe(III) in octahedral

444   symmetry (Eyre and Dickson, 1995), while the other one with IS of 1.12 mm s^{-1} and

445   QS of 2.65 mm s^{-1} was characteristic of high spin Fe(II) (Hofstetter et al., 2003;

446   Kopcewicz et al., 2015). The two doublet components of the IMt-2, NAu-2, SWy-2

447 and ATD samples before CP were all attributed to different fractions of Fe(III) and

448 Fe(II) in the aluminosilicate crystals, respectively. Before CP, the Fe(II) fraction in the

449 IMt-2, NAu-2, SWy-2 and ATD samples were 34.0 %, 12.9 %, 18.3 % and 29.0 %,

450 respectively (Figure 6 a, c, e and g). Furthermore, the spectra of the ATD sample

451 before CP showed not only two central quadrupole doublets, but also one MHS sextet

452 with IS of 0.39 mm s^{-1}, QS of −0.13 mm s^{-1} and H$_f$ of 51.1 T. The MHS sextet, which

453 shared 31.8 % of the whole area, could be ascribed to α-Fe$_2$O$_3$ (Kopcewicz and

454 Kopcewicz et al., 1991), in agreement with the TEM analysis and "free-Fe"

455 measurement as mentioned previously.

456 After CP, the Fe(II) content of the samples decreased to 31.5 %, 11.6 %, 17.1% and

457 10.9%, respectively, for IMt-2, NAu-2, SWy-2 and ATD (Figure 6 b, d, f and h). It

458 was supposed that the Fe(II) release is more energetically favorable than one of Fe(III)

459 due to the bond strength. As to the ATD sample after CP (Figure 6 h), not only did the

460 Fe(II) fraction decrease from 29.0% to 10.9%, but also the Fe(III) fraction in the

461 aluminosilicates decreased from 39.0% to 33.0%. Meanwhile, the α-Fe$_2$O$_3$ fraction

462 was not significantly changed (31.8% vs. 32.3%). As discussed previously, the Fe

463 mobilization was dependent on the specific chemical bonds. The Fe$_D$ phase in

464 α-Fe$_2$O$_3$ with the strong Fe−O bond was less liable than that embedded in the

465 aluminosilicate lattice (Strehlau et al., 2017). It was well documented that the Fe

466 replacing alkaline elements as the interlayer ions was easy to be mobilized than the Fe

467 bound by covalent bonds in the aluminosilicate matrix (Luo et al., 2005; Cwiertny et

468 al., 2008; Journet et al., 2008). Therefore, the Fe in the aluminosilicate fraction of the

469 mineral particles exhibited varied iron solubility.

470 Particularly, a new quadrupole doublet with IS of 0.67 mm s^{-1} and QS of 1.21 mm

471 s^{-1} was observed in the spectra of the ATD sample after CP (Figure 6 h), which shared

472 23.8% of the total area, and was possibly indicative of the Fe(III) oxide hybridized in

473 the aluminosilicate matrix (Kopcewicz and Kopcewicz, 1991). The "free-Fe"

474 measurement have indicated that the Fe_A fraction of ATD increased by 20.4% after CP,

475 so that this Fe phase was most likely to be amorphous Fe(III) hybridized with Al/Si.

476 In the terms of the other samples after CP, the magnetic signal of the newly formed

477 Fe(III) phase was not detected. It was probably due to the newly formed Fe fractions

478 were not available at sufficiently high level to be clearly resolved by the Mössbauer

479 spectroscopy, and/or the slight signal drift and the poor signal to noise ratio made an

480 unambiguous identification difficult. Herein, the newly formed amorphous Fe(III)

481 phase was supposed to be a reactive Fe-bearing component, of which may contribute

482 significantly to the SO_2 uptake even at a low level.

483 **Figure 6**

484 **3.5 The dissolution-precipitation cycle of the mineral Fe during CP**

485 During the simulated CP experiments, the concentrations of total dissolved Fe (Fe_s),

486 dissolved Fe(II) and Fe(III) released from the particles as a function of time are shown

487 in Figure 7. Similar dissolution trends were observed for all of the samples. One can

488 see that the suspensions at pH 2 induced a rapid increase of Fe_s. Once increasing the

489 pH from 2 to 5 resulted in a rapid and almost complete removal of Fe_s. In fact, only a

490 rather small fraction of the Fe in dusts could be dissolved at pH above 4 (Zuo and

491 Hoigne, 1992). The dissolved Fe precipitated rapidly as insoluble deposit at pH 5.

492 When the suspension pH was again reduced to 2, a steep increase in the Fe_s

493 concentration was measured once again. The fast Fe release was due to the

494 redissolution of the Fe-rich precipitates, which was proposed to be reactive Fe phases

495 (Shi et al., 2009; Shi et al., 2015). Such highly soluble Fe-bearing precipitates have

496 been observed under the TEM, as well as the "free Fe" measurement and Mössbauer

497   characterization.

498   **Figure 7**

499   For each pH cycle during the simulated CP experiment, the overall changes of total

500   released Fe concentrations were reproducible. The Fe ion on the particle surfaces

501   would experience a continuous dissolution-precipitation-redissolution-reprecipitation

502   process when the pH cycles between pH 2 and pH 5 (cloud-aerosol modes). During

503   this process, the Fe(II) fraction would be transformed to Fe(III). The results shown

504   herein suggested that CP could significantly modify Fe partitioning between dissolved

505   and particulate phases in the real atmosphere. Not only did the increase of specific

506   surface area contribute to the enhanced sulfate formation, but also the highly reactive

507   Fe on the particle surfaces yielded during CP were also responsible for the higher SO_2

508   uptake on the particles after CP.

509   When investigating the NAu-2 sample, once the pH of the clear solution increased

510   from 2 to 5-6, the Fe-bearing nanoparticles separated out from the solution rapidly

511   and precipitate out slowly. It developed an initial yellow color and then an orange

512   colored suspension. The TEM images of the precipitated particles are shown in Figure

513   8. The particles could be categorized into two different types. One type of particle

514   could be characterized as hundreds of nanometers in size, with low Fe but high Si/Al

515   content. The other type displayed particle sizes nearly 1 micrometer, and were Fe-rich

516   but contained a smaller amount of Si/Al components. These bigger particles were

517   ambiguously identified as $Na_{0.42}Fe_3Al_6B_{309}Si_6O_{18}(OH)_{3.65}$ (PDF: 89-6506) on the

518   basis of the EDX data and SAED analysis. It is likely that the Al/Si elements also

519   precipitated out along with the Fe.

520   **Figure 8**

521   The Mössbauer spectra of the precipitated Fe-rich particles are shown in Figure 9.

522   Two central doublets were distinguished, with one (48.4%) of IS = 0.45 mm s^{-1}, QS =

523   0.75 mm s^{-1}, and the other (51.6%) of IS = 0.24 mm s^{-1}, QS = 0.76 mm s^{-1}. Both of

524   the two doublet components could be attributed to the Fe(III) fraction in the

525   aluminosilicates (Kopcewicz et al., 2015). The results were in good agreement with

526   the TEM observation, which showed that most of these Fe particles were mostly

527   present as the Fe(III) hybridized with Al/Si. The particle size distributions in the

528   suspensions were also determined by dynamic light scattering, as shown in Figure 10.

529   When pH was lower than 2.0, the particles seemed to stabilize below 10 nm in size.

530   These Fe colloids were thought to be a source of soluble Fe (Janney et al., 2000).

531   Once pH increased, the size of precipitated particles quickly increased, even to

532   micro-scale, and the suspension was featured with a polydispersed size distribution.

533   Conclusively, the precipitated Fe were mainly Fe(III) with weak crystal structure

534   and/or ferrihydrite nanoparticle hybridized with Al/Si, which were possibly

535   transformed from the Fe hosted in the aluminosilicate matrix of the particles. The

536   particle surfaces after CP were coated by these reactive Fe to provide more surface

537   OH species, resulting in enhanced SO_2 uptake.

538   **Figure 9**

539   **Figure 10**

540 **4 Conclusion and implication**

541   Transition metal ions, especially Fe(III), could catalyze SO_2 oxidation rapidly in

542   cloud drops (Harris et al., 2013). This study further confirmed that SO_2 uptake on the

543   mineral particles could be greatly enhanced by CP, possibly more than described

544   previously. The higher uptake coefficient of the particles after CP was not only due to

545   increased surface area, but also resulted from the chemical modification of the particle

surfaces. The "free-Fe" and Mössbauer analysis suggested that CP triggered newly

formation of amorphous Fe particles on the surfaces, of which were mostly

transformed from the Fe hosted in the aluminosilicate matrix. TEM showed that the

amorphous Fe(III) and/or ferrihydrite nanoparticle were hybridized with Al/Si. In

general, the acidity fluctuation during CP enables the dissolution-precipitation cycles

of mineral Fe to yielded more reactive Fe, resulting in more SO_2 uptake on the

particle surfaces. More SO_2 adsorption further increases the surface acidity of dust

particles, in turn leading to higher Fe solubility; again, more sulfate formation. It was

thus proposed that there is a positive feedback relative to SO_2 update and iron

mobilized from mineral particles during CP, therefore enhanced sulfate formation

greatly.

Our results also serve to explain high sulfate loading in fog-haze episodes of China.

It has been recommended that sulfate contributed significantly to the explosive

growth of fine particles, thus exacerbating severe fog-haze development (Kasibhatla

et al., 1997; Nie et al., 2014; Barrie et al., 2016). Haze and fog within an episode was

often found to transform each other at a short time due to the diurnal variation of RH,

whereby the haze-fog transition was probably analogous to the aerosol-cloud

interaction. Water content of aerosol or fog drops was regulated by RH, and thus

allowed the particle acidity fluctuation. Although the aerosol acidity could not be

accurately determined from field measurements or calculated using the

thermodynamic model, we recognized that the large pH fluctuations between the

haze-fog modes could significantly modify the microphysical properties of mineral

particles, and triggered formation of reactive Fe particles and thus accelerated sulfate

formation via a self-amplifying process, contributing to explosive growth of fine

particles at the initial stage of fog-haze events. The data presented herein also

571 highlight that CP provide more bioavailable iron from mineral particle than one

572 expected previously, of which is a key speciation to promote oceanic primary

573 productivity. Results of this study could partly explain the missing source of sulfate

574 and improve agreement between models and field observations.

575 Additionally, previous studies indicated that Fe in pyrogenic aerosols was always

576 presented as liable Fe, such as ferric sulfate and aggregated nanocrystals of magnetite

577 (Fe_3O_4) (Fu et al., 2012), and displayed higher Fe solubility compared to dust

578 (Desboeufs et al., 2005; Sedwick et al., 2007; Ito et al., 2019). Alexander et al.

579 demonstrated that the sulfate formed through metal catalysis was highest over the

580 polluted industrial regions of northern Eurasia, suggesting that the increasing

581 importance of the metal-catalyzed S(IV) oxidation pathway due to anthropogenic

582 emissions (Alexander et al, 2009). With the rapid development of industry and

583 agriculture, the pyrogenic Fe-containing aerosols are indispensable contributors to the

584 atmospheric Fe load in China. Thus, the acidic solution at pH 2 and high sulfate

585 loading of fine particles in severe fog-haze events of China might be more relevant to

586 Fe-containing combustion aerosols than mineral dust. Based on the current findings,

587 not only the potential influences of cloud liquid water content, light, and organic

588 ligands, but also the solubility and speciation of Fe in pyrogenic aerosols will be

589 considered during the simulated CP experiments in the future. A more detailed

590 understanding of the iron-sulfur cycle during CP is therefore critical to estimate

591 accurately the contribution of CP to global sulfate loading and its impact on the

592 climate.

Author contributions. Z.W., H.F. and J.C. designed the experiments, Z.W., T.W., H.F. and L.Z. performed the laboratory experiments. H.F., J.C., L.Z. and V.G. contributed reagents/analytic tools. C.G., V.G. and M.T. gave some valuable suggestions in designing the experiments. Z.W., T.W. and H.F. analyzed data. Z.W. and H.F. wrote the manuscript, with inputs from all coauthors.

Competing interests. The authors declare no conflict of interest.

Acknowledgments. This work was supported by National Natural Science Foundation of China (Nos. 91744205, 21777025, 21577022, 21177026), National Key R&D Program of China (2016YFC0202700), and Opening Project of Shanghai Key Laboratory of Atmospheric Particle Pollution and Prevention.

References

Alexander, B., Park, R. J., Jacob, D. J., and Gong, S.: Transition metal-catalyzed oxidation of atmospheric sulfur: Global implications for the sulfur budget, J. Geophys. Res., 114, D02309, 2009.

Andreae, M. O., and Rosenfeld, D.: Aerosol-cloud-precipitation interactions. Part 1. The nature and sources of cloud-active aerosols, Earth Sci. Rev., 89, 13-41, 2008.

Baker, A. R., and Croot, P. L.: Atmospheric and marine controls on aerosol iron solubility in seawater, Mar. Chem., 120, 4-13, 2010.

Barrie, L. A., Yi, Y., Leaitch, W. R., Lohmann, U., Kasibhatla, P., Roelofs, G. J., Wilson, J., McGovern, F., Benkovitz, C., Méliéres, M. A., Law, K., Prospero, J., Kritz, M., Bergmann, D., Bridgeman, C., Chin, M., Christensen, J., Easter, R., Feichter, J., Land, C., Jeuken, A.,

Kjellström, E., Koch, D., and Rasch, P.: A comparison of large-scale atmospheric sulphate aerosol models (COSAM): Overview and highlights, Tellus B, 53, 615-645, 2016.

Behra, P., Sigg, L., and Stumm, W.: Dominating influence of NH_3 on the oxidation of aqueous SO_2: the coupling of NH_3 and SO_2 in atmospheric water, Atmos. Environ., 23, 2691-2707, 1989.

Cheng, Y. F., Zheng, G. J., Wei, C., Mu, Q., Zheng, B., Wang, Z. B., Gao, M., Zhang, Q., He, K. B., Carmichael, G., Poschl, U., and Su, H.: Reactive nitrogen chemistry in aerosol water as a source of sulfate during haze events in China, Sci. Adv., 2, 1-11, 2016.

Claquin, T., Schulz, M., and Balkanski, Y. J.: Modeling the mineralogy of atmospheric dust sources, J. Geophys. Res.-Atmos., 104, 22243-22256, 1999.

Cwiertny, D. M., Baltrusaitis, J., Hunter, G. J., Laskin, A., Scherer, M. M., and Grassian, V. H.: Characterization and acid-mobilization study of iron-containing mineral dust source materials, J. Geophys. Res.-Atmos., 113, D05202, 2008.

Deguillaume, L., Desboeufs, K. V., Leriche, M., Long, Y., and Chaumerliac, N.: Effect of iron dissolution on cloud chemistry: from laboratory measurements to model results, Atmos. Pollut. Res., 1, 220-228, 2010.

Desboeufs, K. V., Losno, R., and Colin, J. L.: Factors influencing aerosol solubility during cloud processes, Atmos. Environ., 35, 3529-3537, 2001.

Desboeufs, K. V., Sofikitis, A., Losno, R., Colin, J. L., and Ausset, P.: Dissolution and solubility of trace metals from natural and anthropogenic aerosol particulate matter, Chemosphere, 58, 195-203, 2005.

Eyre, J. K., and Dickson, D. P. E.: Mössbauer spectroscopy analysis of iron-containing minerals in the Chinese loess, J. Geophys. Res., 100, 17925-17930, 1995.

Faust, B. C., Hoffmann, M. R., and Bahnemann, D. W.: Photocatalytic oxidation of sulfur dioxide in aqueous suspensions of α-Fe_2O_3, J. Phys. Chem., 93, 6371-6381, 1989.

Fu, H. B., Wang, X., Wu, H. B., Yin, Y., and Chen, J. M.: Heterogeneous uptake and oxidation of SO_2 on iron oxides, J. Phys. Chem. C, 111, 6077-6085, 2007.

Fu, H. B., Lin, J., Shang, G. F., Dong, W. B., Grassian, V. H., Carmichael, G. R., Li, Y., and Chen, J. M.: Solubility of iron from combustion source particles in acidic media linked to iron speciation, Environ. Sci. Technol., 46, 11119-11127, 2012.

Formenti, P., Rajot, J. L., Desboeufs, K., Caquineau, S., Chevaillier, S., Nava, S., Gaudichet, A., Journet, E., Triquet, S., Alfaro, S., Chiari, M., Haywood, J., Coe, H., and Highwood, E.: Regional variability of the composition of mineral dust from western Africa: Results from the AMMA SOP0/DABEX and DODO field campaigns, J. Geophys. Res., 113, D00C13, 2008.

George, C., Ammann, M., D'Anna, B., Donaldson D. J., and Nizkorodov, S. A.: Heterogeneous Photochemistry in the Atmosphere, Chem. Rev., 115, 4218-4258, 2015.

Goodman, A. L., Li, P., Usher, C. R., and Grassian, V. H.: Heterogeneous uptake of sulfur dioxide on aluminum and magnesium oxide particles, J. Phys. Chem. A, 105, 6109-6120, 2001.

Harris, E., Sinha, B., Foley, S., Crowley, J. N., Borrmann, S., and Hoppe, P.: Sulfur isotope fractionation during heterogeneous oxidation of SO_2 on mineral dust, Atmos. Chem. Phys.,

12, 4867-4884, 2012.

Harris, E., Sinha, B., van Pinxteren, D., Tilgner, A., Fomba, K. W., Schneider, J., Roth, A., Gnauk, T., Fahlbusch, B., Mertes, S., Lee, T., Collett, J., Foley, S., Borrmann, S., Hoppe, P., and Herrmann, H.: Enhanced role of transition metal ion catalysis during in-cloud oxidation of SO_2, Science, 340, 727-730, 2013.

Herman, L. M. S.: Heterogeneous and homogeneous oxidation of SO_2 in the remote marine atmosphere, Atmos. Environ., 25, 1489-1496, 1991.

Huang, L., Zhao, Y., Li, H., and Chen, Z.: Kinetics of heterogeneous reaction of sulfur dioxide on authentic mineral dust: Effects of relative humidity and hydrogen peroxide, Environ. Sci. Technol., 49, 10797-17805, 2015.

Hofstetter, T. B., Schwarzenbach, R. P., and Haderlein, S. B.: Reactivity of Fe(II) species associated with clay minerals, Environ. Sci. Technol., 37, 519-528, 2003.

Ito, A., Myriokefalitakis, S., Kanakidou, M., Mahowald, N., Scanza, R., Hamilton, D., Baker, A., Jickells,T., Sarin, M., Bikkina, S., Gao, Y., Shelley, R., Buck, C., Landing, W., Bowie, A., Perron, M., Guieu, C., Meskhidze, N., Johnson, M., Feng, Y., Kok, J., Nenes, A. and Duce, R.: Pyrogenic iron: The missing link to high iron solubility in aerosols, Sci. Adv., 5(5), eaau7671, 2019.

Janney, D. E., Cowley, J. M., and Buseck, P. R.: Transmission electron microscopy of synthetic 2-and 6-line ferrihydrite, Clay Clay Miner., 48, 111-119, 2000.

Jickells, T. D., An, Z. S., Andersen, K. K., Baker, A. R., Bergametti, G., Brooks, N., Cao, J. J., Boyd, P. W., Duce, R. A., Hunter, K. A., Kawahata, H., Kubilay, N., laRoche, J., Liss, P. S.,

Mahowald, N., Prospero, J. M., Ridgwell, A. J., Tegen, I., and Torres, R.: Global iron connections between desert dust, ocean biogeochemistry, and climate, Science, 308, 67-71, 2005.

Journet, E., Desboeufs, K. V., Caquineau, S., and Colin, J.-L.: Mineralogy as a critical factor of dust iron solubility, Geophys. Res. Lett., 35, L07805, 2008.

Kadar, E., Fisher, A., Stolpe, B., Calabrese, S., Lead, J., Valsami-Jones, E., and Shi, Z.: Colloidal stability of nanoparticles derived from simulated cloud-processed mineral dusts, Sci. Total. Environ., 466-467, 864-870, 2014.

Kasibhatla, P., Chameides, W. L., and John, J. S.: A three-dimensional global model investigation of seasonal variations in the atmospheric burden of anthropogenic sulfate aerosols, J. Geophys. Res.-Atmos., 102, 3737-3759, 1997.

Kerminen, V. M., Pirjola, L., Boy, M., Eskola, A., Teinila, K., Laakso, L., Asmi, A., Hienola, J., Lauri, A., Vainio, V., Lehtinen, K., and Kulmala, M.: Interaction between SO_2 and submicron atmospheric particles, Atmos. Res., 54, 41-57, 2000.

Kolb, C. E., Cox, R. A., Abbatt, J. P. D., Ammann, M., Davis, E. J., Donaldson, D. J., Garrett, B. C., George, C., Griffiths, P. T., Hanson, D. R., Kulmala, M., McFiggans, G., Pöschl, U., Riipinen, I., Rossi, M. J., Rudich, Y., Wagner, P. E., Winkler, P. M., Worsnop, D. R., and O'Dowd, C. D.: An overview of current issues in the uptake of atmospheric trace gases by aerosols and clouds, Atmos. Chem. Phys., 10, 10561-10605, 2010.

Kong, L. D., Zhao, X., Sun, Z. Y., Yang, Y. W., Fu, H. B., Zhang, S. C., Cheng, T. T., Yang, X., Wang, L., and Chen, J. M.: The effects of nitrate on the heterogeneous uptake of sulfur

dioxide on hematite, Atmos. Chem. Phys., 14, 9451-9467, 2014.

Kopcewicz, B., and Kopcewicz, M.: Mössbauer study of iron-containing atmospheric aerosols, Struct. Chem., 2, 303-312, 1991.

Kopcewicz, B., Kopcewicz, M., and Pietruczuk, A.: The Mössbauer study of atmospheric iron-containing aerosol in the coarse and $PM_{2.5}$ fractions measured in rural site, Chemosphere, 131, 9-16, 2015.

Lafon, S., Rajot, J.-L., Alfaro, S. C., and Gaudichet, A.: Quantification of iron oxides in desert aerosol, Atmos. Environ., 38, 1211-1218, 2004.

Lelieveld, J., and Heintzenberg, J.: Sulfate cooling effect on climate through in-cloud oxidation of anthropogenic SO_2, Science, 258, 117-120, 1992.

Luo, C., Mahowald, N. M., Meskhidze, N., Chen, Y., Siefert, R. L., Baker, A. R., and Johansen, A. M.: Estimation of iron solubility from observations and a global aerosol model, J. Geophys. Res., 110, D23, 2005.

Luo, C., Mahowald, N., Bond, T., Chuang, P. Y., Artaxo, P., Siefert, R., Chen, Y., and Schauer, J.: Combustion iron distribution and deposition, Global Biogeochem. Cycles, 22, GB1012, 2008.

Luria, M., and Sievering, H.: Heterogeneous and homogeneous oxidation of SO_2 in the remote marine atmosphere, Atmos. Environ., 25, 1489-1496, 1991.

Ma, Q., He, H., and Liu, Y.: In situ DRIFTS study of hygroscopic behavior of mineral aerosol, J. Environ. Sci., 22, 555-560, 2010.

Mackie, D. S.: Simulating the cloud processing of iron in Australian dust: pH and dust

concentration, Geophys. Res. Lett., 32, L06809, 2005.

Mahowald, N. M., Baker, A. R., Bergametti, G., Brooks, N., Duce, R. A., Jickells, T. D., Kubilay, N., Prospero, J. M., and Tegen, I.: Atmospheric global dust cycle and iron inputs to the ocean. Global Biogeochem. Cycles, 19, GB4025, 2005.

Maters, E. C., Delmelle, P., and Bonneville, S.: Atmospheric processing of volcanic glass: Effects on iron solubility and redox speciation. Environ. Sci. Technol., 50 (10), 5033-5040, 2016.

Meskhidze, N.: Iron mobilization in mineral dust: Can anthropogenic SO_2 emissions affect ocean productivity? Geophys. Res. Lett., 30, 1-2, 2003.

Nanayakkara, C. E., Pettibone, J., and Grassian, V. H.: Sulfur dioxide adsorption and photooxidation on isotopically-labeled titanium dioxide nanoparticle surfaces: Roles of surface hydroxyl groups and adsorbed water in the formation and stability of adsorbed sulfite and sulfate, Phys. Chem. Chem. Phys., 14, 6957-6966, 2012.

Nie, W., Ding, A. J., Wang, T., Kerminen, V., George, C., Xue, L. K., Wang, W. X., Zhang, Q. Z., Petäjä, T., Qi, X. M., Gao, X. M., Wang, X. F., Yang, X. Q., Fu, C. B., and Kulmala, M.: Polluted dust promotes new particle formation and growth, Sci. rep., 4, 6634, 2014.

Peak, D., Ford, R. G., and Sparks, D. L.: An in situ ATR-FTIR investigation of sulfate bonding mechanisms on goethite, J. Colloid Interface Sci., 218, 289-299, 1999.

Pruppacher, H. R., Jaenicke, R.: The processing of water-vapor and aerosols by atmospheric clouds, a global estimate, Atmos. Res., 38, 283-295, 1995.

Rubasinghege, G., Lentz, R. W., Scherer, M. M., and Grassian, V. H.: Simulated atmospheric

processing of iron oxyhydroxide minerals at low pH: roles of particle size and acid anion in iron dissolution, Proc. Natl. Acad. Sci. U. S. A., 107, 6628-6633, 2010.

Sedwick, P. N., Sholkovitz, E. R., and Church, T. M.: Impact of anthropogenic combustion emissions on the fractional solubility of aerosol iron: Evidence from the Sargasso Sea, Geochem. Geophys. Geosyst., 8, Q10Q06, 2007.

Shi, Z., Bonneville, S., Krom, M. D., Carslaw, K. S., Jickells, T. D., Baker, A. R., and Benning, L. G.: Iron dissolution kinetics of mineral dust at low pH during simulated atmospheric processing, Atmos. Chem. Phys., 11, 995-1007, 2011.

Shi, Z., Krom, M. D., Bonneville, S., Baker, A. R., Jickells, T. D., and Benning, L. G.: Formation of iron nanoparticles and increase in iron reactivity in mineral dust during simulated cloud processing, Environ. Sci. Technol., 43, 6592-6596, 2009.

Shi, Z., Krom, M. D., Bonneville, S., Baker, A. R., Bristow, C., Drake, N., Mann, G., Carslaw, K., McQuaid, J. B., Jickells, T., and Benning, L. G.: Influence of chemical weathering and aging of iron oxides on the potential iron solubility of Saharan dust during simulated atmospheric processing, Global Biogeochem. Cycles, 25, GB2010, 2011.

Shi, Z., Krom, M. D., Bonneville, S., and Benning, L. G.: Atmospheric processing outside clouds increases soluble iron in mineral dust, Environ. Sci. Technol., 49, 1472-1477, 2015.

Siefert, R. L., Johansen, A. M., Hoffmann, M. R., and Pehkonen, S. O.: Measurements of trace metal (Fe, Cu, Mn, Cr) oxidation states in fog and stratus clouds, J. Air Waste Manage., 48(2), 128–143, 1998.

Spokes, L. J., Jickells, T. D., and Lim, B.: Solubilization of aerosol trace-metals by cloud

processing - a laboratory study, Geochim. Cosmochim. Acta., 58, 3281-3287, 1994.

Strehlau, J. H., Schultz, J. D., Vindedahl, A. M., Arnold, W. A., and Penn, R. L.: Effect of nonreactive kaolinite on 4-chloronitrobenzene reduction by Fe(II) in goethite-kaolinite heterogeneous suspensions, Environ. Sci.: Nano, 4, 325-334, 2017.

Sun, Y. L., Jiang, Q., Wang, Z. F., Fu, P. Q., Li, J., Yang, T., and Yin, Y.: Investigation of the sources and evolution processes of severe haze pollution in Beijing in January 2013, J. Geophys. Res.-Atmos., 119, 4380-4398, 2014.

Ullerstam, M., Johnson, M. S., Vogt, R., and Ljungstrom, E.: DRIFTS and Knudsen cell study of the heterogeneous reactivity of SO_2 and NO_2 on mineral dust, Atmos. Chem. Phys., 3, 2043-2051, 2003.

Usher, C. R., Al-Hosney, H., Carlos-Cuellar, S., and Grassian, V. H.: A laboratory study of the heterogeneous uptake and oxidation of sulfur dioxide on mineral dust particles, J. Geophys. Res.-Atmos., 107, 161-169, 2002.

Usher, C. R., Michel, A. E., and Grassian, V. H.: Reactions on mineral dust, Chem. rev., 103, 4883-4940, 2003.

Viollier, E., Inglett, P. W., Hunter, K., Roychoudhury, A. N., and Van Cappellen, P.: The ferrozine method revisited: Fe(II)/Fe(III) determination in natural waters, Appl. Geochem., 15, 785-790, 2000.

Wang, G., Wang, H., Yu, Y., Gao, S., Feng, J., Gao, S., and Wang, L.: Chemical characterization of water-soluble components of PM_{10} and $PM_{2.5}$ atmospheric aerosols in five locations of Nanjing, China, Atmos. Environ., 37, 2893-2902, 2003.

Wang, Y., Zhang, Q., Jiang, J., Zhou, W., Wang, B., He, K., Duan, F., Zhang, Q., Philip, S., and Xie, Y.: Enhanced sulfate formation during China's severe winter haze episode in January 2013 missing from current models, J. Geophys. Res.-Atmos., 119, 10425-10440, 2014.

Wu, L. Y., Tong, S. R., Wang, W. G., and Ge, M. F.: Effects of temperature on the heterogeneous oxidation of sulfur dioxide by ozone on calcium carbonate, Atmos. Chem. Phys., 11, 6593-6605, 2011.

Wurzler, S., Reisin, T. G., and Levin, Z.: Modification of mineral dust particles by cloud processing and subsequent effects on drop size distributions, J. Geophys. Res.-Atmos., 105, 4501-4512, 2000.

Yang, W., He, H., Ma, Q., Ma, J., Liu, Y., Liu, P., and Mu, Y.: Synergistic formation of sulfate and ammonium resulting from reaction between SO_2 and NH_3 on typical mineral dust, Phys. Chem. Chem. Phys., 18, 956-964, 2016.

Yang, W., Zhang, J., Ma, Q., Zhao, Y., Liu, Y., and He, H.: Heterogeneous reaction of SO_2 on manganese oxides: the effect of crystal structure and relative humidity, Sci. rep., 7, 4550, 2017.

Zhang, X., Zhuang, G., Chen, J., Wang, Y., Wang, X., An, Z., and Zhang, P.: Heterogeneous reactions of sulfur dioxide on typical mineral particles, J. Phys. Chem. B, 110, 12588-12596, 2006.

Zhao, X., Kong, L., Sun, Z., Ding, X., Cheng, T., Yang, X., and Chen, J.: Interactions between heterogeneous uptake and adsorption of sulfur dioxide and acetaldehyde on hematite, J.

Phys. Chem. A, 119, 4001-4008, 2015.

Zhao, Y., Liu, Y., Ma, J., Ma, Q., and He, H.: Heterogeneous reaction of SO_2 with soot: The roles of relative humidity and surface composition of soot in surface sulfate formation, Atmos. Environ., 152, 465-476, 2017.

Zhu, X., Prospero, J. M., Savoie, D. L., Millero, F. J., Zika, R. G., and Saltzman, E. S.: Photoreduction of iron(III) in marine mineral aerosol solutions, J. Geophys. Res.-Atmos., 98, 9039-9046, 1993.

Zhuang, G. S., Yi, Z., Duce, R. A., and Brown, P. R.: Link between iron and sulfur cycles suggested by detection of Fe(II) in remote marine aerosols, Nature, 355 (6360), 537-539, 1992.

Zuo, Y. G., and Hoigne, J.: Formation of hydrogen-peroxide and depletion of oxalic-acid in atmospheric water by photolysis of iron(III) oxalato complexes, Environ. Sci. Technol., 26, 1014-1022, 1992.

Captions of Figures and Tables

Figure 1. Comparison of morphologies and chemical properties for samples collected before and after CP using TEM. The dotted circles indicate the positions of the electron beam for the HRTEM images and SAED patterns. Elements of the detected parts of individual particles are also presented. Square brackets indicate mass percent of iron. The iron species were identified by the Miller indices and the SAED patterns. (a) IMt-2 particles characterized by high fractions of Al and Si, along with other crustal elements including Mg, K and Fe. (b) IMt-2 particles after CP were almost all less than 1μm in size. Some Fe-rich particles with less Si and Al were observed on nanoscale dimension. (c) NAu-2 particles with high Fe/Si-ratios, contain Mg, Al and Ca elements. (d) NAu-2 particles after CP were much smaller than the ones before CP. Some ferrihydrite clusters were observed and were attached on the surface of the NAu-2 particles after CP. (e) Typical SWy-2 particles were Al/Si-rich, containing Fe, Mg and Ca elements. (f) TEM images of the SWy-2 particles after CP appeared smaller than the particles before CP. (g) The Si/Al-rich crystal in ATD particles was aluminosilicate with low content of Fe, and a typical of the α-Fe_2O_3 particles (PDF: 33-664) was found to attach onto the aluminosilicate surface. (h) The pseudohexagonal nanoparticles were observed to on the surface of α-Fe_2O_3 crystal among the ATD particles. The SAED lattice constant of these nanoparticles were found to be very close to that of 2-line ferrihydrite.

Figure 2. Comparison of the DRIFT spectra of mineral dust samples upon exposure to SO_2 for 45 min before and after CP. Data for IMt-2 (a and b), NAu-2 (c and d), SWy-2 (e and f), ATD (g and h), are shown in the ranges of 4000 to 1250 cm^{-1} and 1250 to 1000 cm^{-1}, respectively.

Figure 3. Comparison of the integrated areas on DRIFTS spectra in the range of 1250-1000 cm^{-1} for the sulfate species formed on the samples before and after CP.

Table 1. Sulfate formation rates and uptake coefficients of SO_2 on particle samples before and after CP.

Figure 4. Comparison of the sulfate formation rates as a function of pH cycle.

Figure 5. The fractions of "free-Fe" (Fe_A and Fe_D) and "structural-Fe" were measured by the chemical CBD extractions for the samples before and after CP. Results are present as relative percentage of Fe_T.

Figure 6. Mössbauer spectroscopy measured for samples. IMt-2 before and after CP (a and b), NAu-2 before and after CP (c and d), SWy-2 before and after CP (e and f), ATD before and after CP (g and h). Experimental data were fit using a least-squares fitting-program. The IS values were relative to α-Fe at RT. Prominent spectral features associated with different iron species are indicated.

Figure 7. The concentrations of Fe_s, dissolved Fe(II) and Fe(III) in the suspensions measured over 144 h in the solution cycled between pH 2 and pH 5 for IMt-2 (a), NAu-2 (b), SWy-2 (c) and ATD (d), respectively.

Figure 8. TEM images of the newly formed particles in the precipitation experiment. Based on the TEM-EDX measurement and SAED analysis, these particles could be categorized into two different types, which were circled in Figure 8 a. The typical sizes of the first type were hundreds of nanometers. The enlarged images are displayed in Figure 8 b, c and d. The insert EDX data and SAED image confirmed that they were poor crystalline aluminosilicate with low Fe but high Si/Al content. The second type (Figure 8 e, f and g) were Fe-rich but with less amount of Si/Al, which were nearly 1 micrometer in size. Based on the EDX data and the SAED

analysis, these bigger particles were ambiguously identified as $Na_{0.42}Fe_3Al_6B_{309}Si_6O_{18}(OH)_{3.65}$ (PDF: 89-6506).

Figure 9. Mössbauer spectroscopy measured at RT for the neo-formed particles collected in the precipitation experiment.

Figure 10. During the precipitation experiment, the particle size distributions in the suspensions were determined by dynamic light scattering. The presented size distributions are characteristic of neo-formed nanoparticles or microparticles as the suspension pH raised from 1.0 to 3.8.

Figure 1
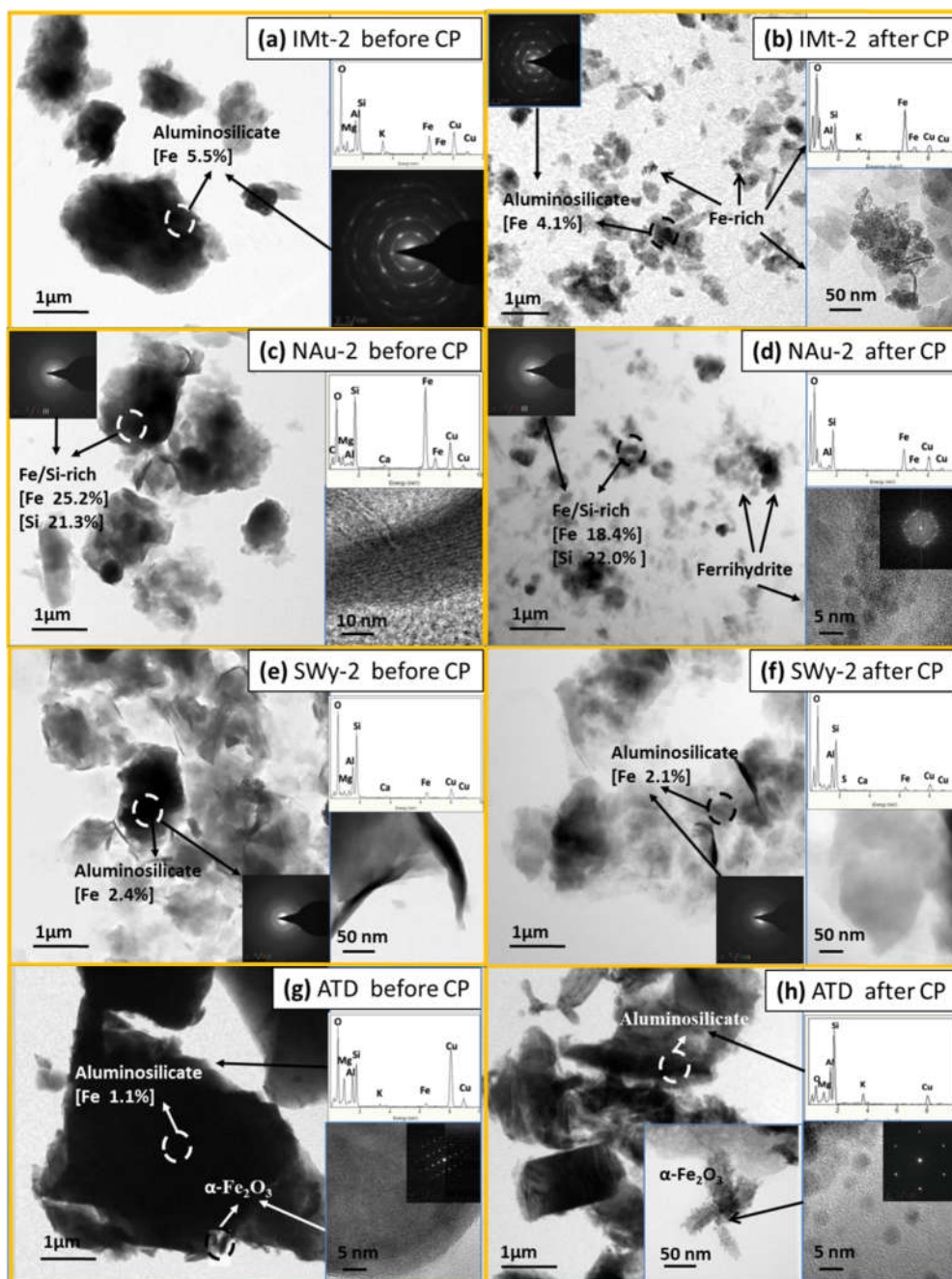
Figure 2
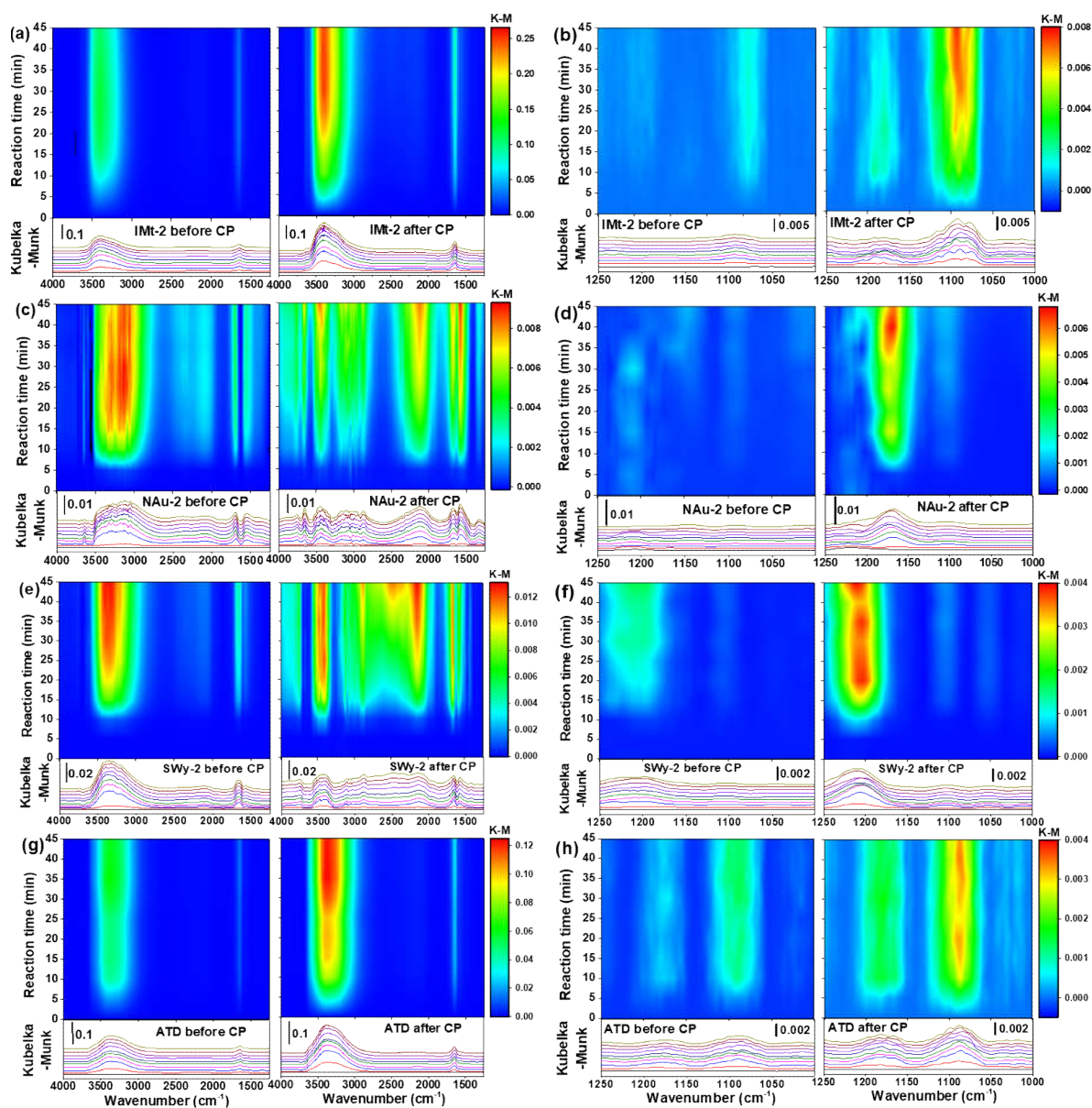
Figure 3
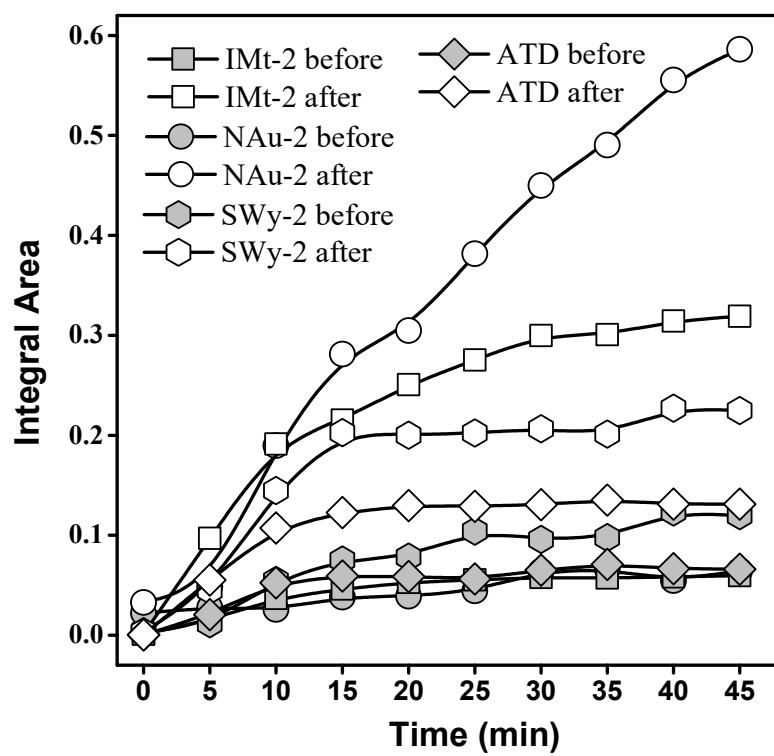
Table 1

Samples	A_{BET} (m^2)	Sulfate formation rate (ions s^{-1}) ($\times 10^{10}$)	$A_{geometric}$ (m^2) ($\times 10^{-5}$)	γ_{BET} ($\times 10^{-12}$)	$\gamma_{geometric}$ ($\times 10^{-7}$)
IMt-2 before CP	0.770	6.13	1.95	2.62	1.03
IMt-2 after CP	1.640	28.72	1.95	5.76	4.85
NAu-2 before CP	0.790	1.80	1.95	0.75	0.30
NAu-2 after CP	3.749	34.57	1.95	3.06	5.83
SWy-2 before CP	0.906	10.20	1.95	3.70	1.72
SWy-2 after CP	1.631	27.19	1.95	5.49	4.59
ATD before CP	0.166	8.11	1.95	16.05	1.37
ATD after CP	0.241	16.33	1.95	22.33	2.76

Figure 4
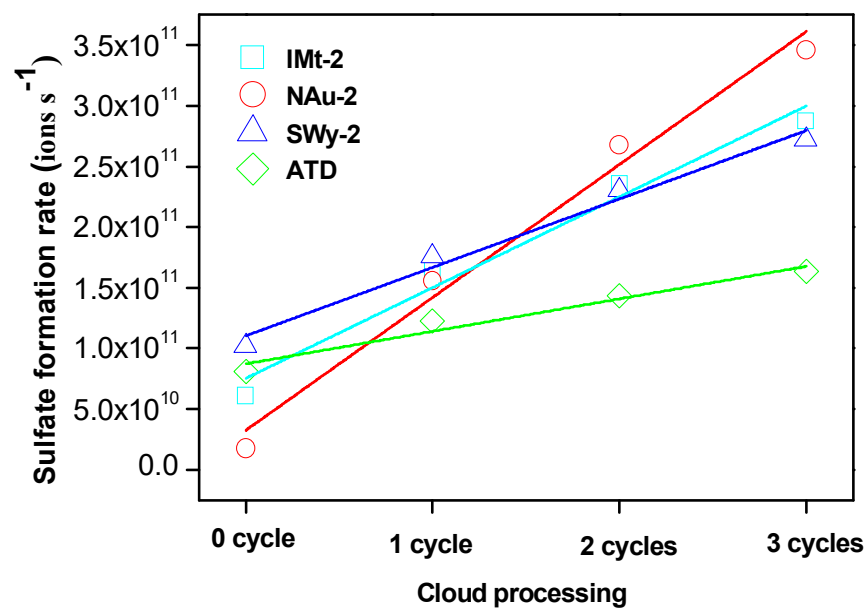
Figure 5
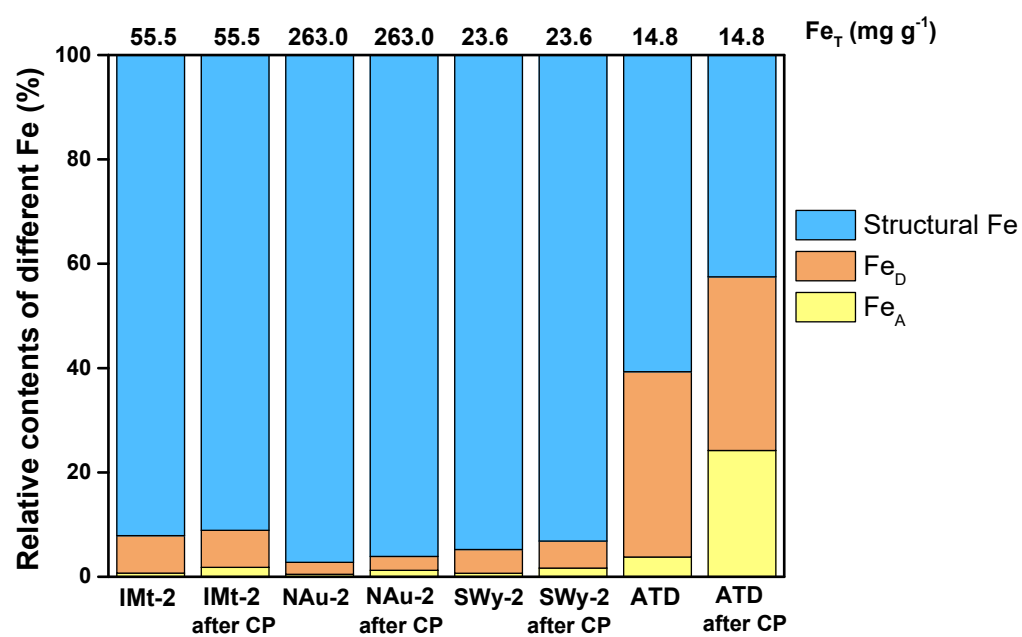
Figure 6
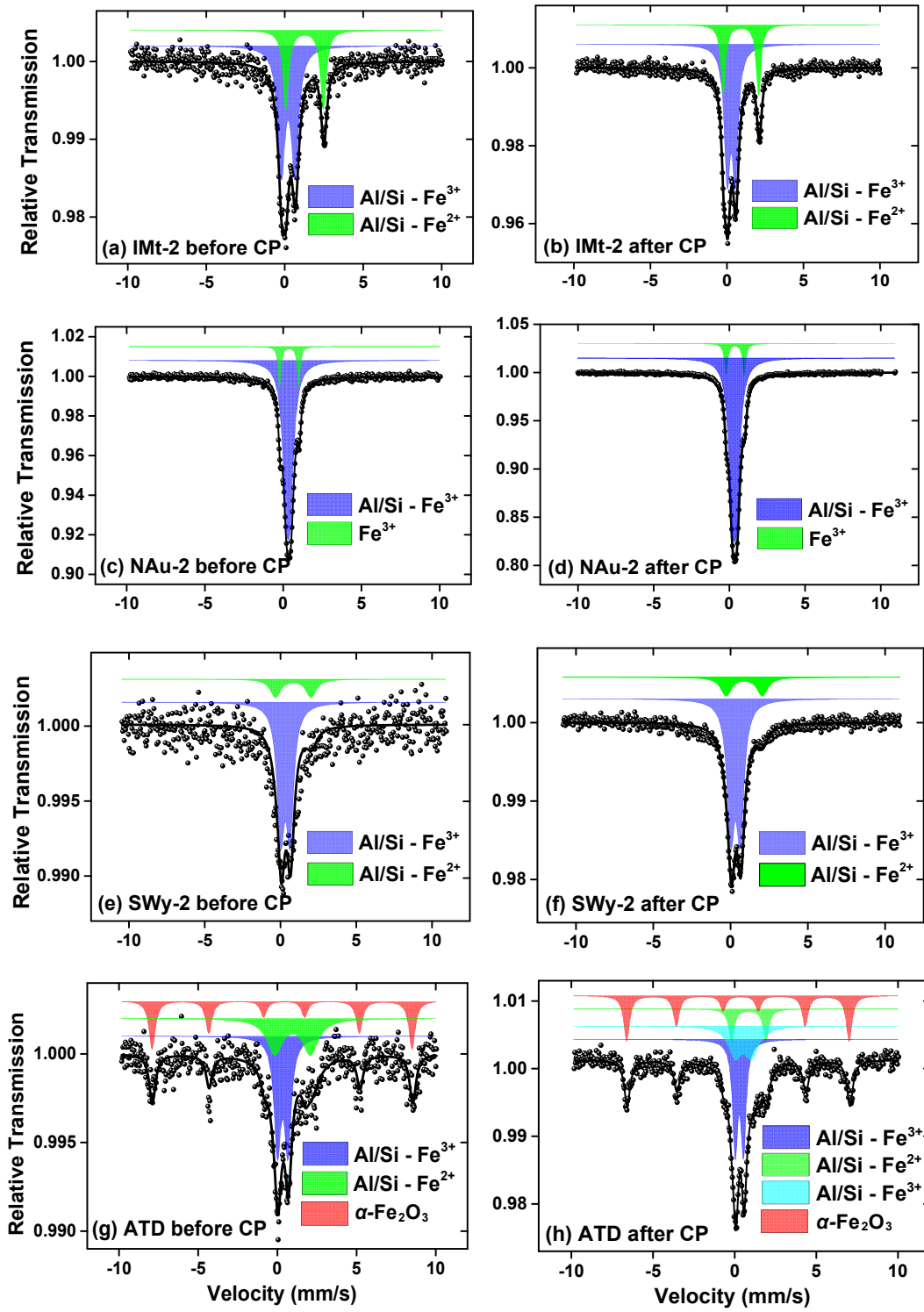
Figure 7
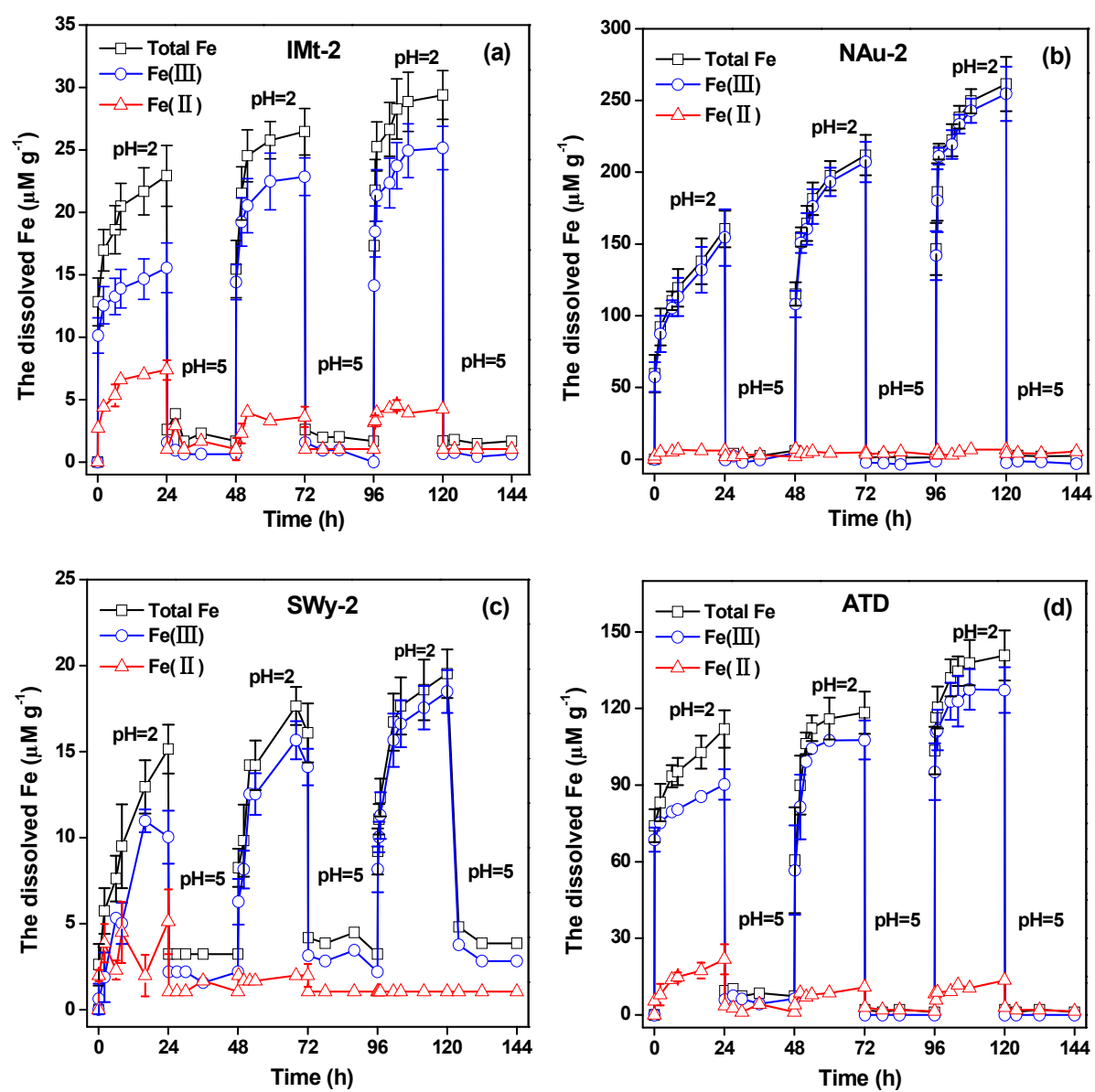
Figure 8

Figure 9

Figure 10